Journal of Materials Chemistry A

PAPER

View Article Online
View Journal | View Issue

Cite this: J. Mater. Chem. A, 2014, 2, 7446

High voltage sulphate cathodes $Li_2M(SO_4)_2$ (M = Fe, Mn, Co): atomic-scale studies of lithium diffusion, surfaces and voltage trends†

John M. Clark,[a] Christopher Eames,[a] Marine Reynaud,‡[b] Gwenaëlle Rousse,[cd] Jean-Noël Chotard,[b] Jean-Marie Tarascon[d] and M. Saiful Islam*[a]

Received 6th December 2013
Accepted 24th March 2014

DOI: 10.1039/c3ta15064j

www.rsc.org/MaterialsA

The search for high voltage cathodes for lithium-ion batteries has led to recent interest in the monoclinic $Li_2Fe(SO_4)_2$ material which has a voltage of 3.83 V *vs.* lithium, the highest recorded for a fluorine-free iron-based compound. Here we investigate the defect, surface and lithium migration properties of the $Li_2M(SO_4)_2$ (M = Fe, Mn, Co) materials using combined atomistic modelling and density functional theory (DFT) techniques. All intrinsic defect types including Li/M antisite disorder are found to be of high energy, suggesting insignificant concentrations. Low activation energies are found for lithium migration along the *a*-axis channels giving rise to long-range 1D diffusion, which are supported by molecular dynamics (MD) simulations. For the crystal morphology a significant surface area is exposed to these 1D diffusion channels, which would allow facile Li insertion and extraction. Using DFT simulations we reproduce the high voltage of the $Li_2Fe(SO_4)_2$ material in accord with electrochemical data and also examine local structural distortions on lithium extraction.

1. Introduction

The search for alternative cathode materials to replace the layered $LiCoO_2$ system conventionally used within rechargeable lithium batteries has generated considerable research activity.[1–7] The Co-based materials pose problems associated with cost, safety and sustainability, particularly for large-scale applications (such as electric vehicles and grid storage). An avenue that has been heavily probed in the quest for new materials involves the combination of abundant Fe and stable phosphate groups (PO_4^{3-}), with most interest focused on olivine-structured $LiFePO_4$.[1–5,8] In recent studies other polyanion framework compounds have been investigated as alternative cathode materials including the following: Li_2FeSiO_4,[9,10] $LiFeBO_3$,[11] $LiFeSO_4F$,[12–15] Li_2FePO_4F,[16] $Li_2FeP_2O_7$,[17] and $LiFeSO_4OH$.[15,18–20]

More recently, the newly synthesised lithium iron sulphate, with the composition $Li_2Fe(SO_4)_2$, was found to display a theoretical capacity of 102 mA h g^{-1} and a high potential of 3.83 V *vs.* Li/Li^+ for the Fe^{2+}/Fe^{3+} redox couple, which is the highest reported voltage for a fluorine-free iron-based compound.[21] Further studies of the structural and transport properties will provide useful insights into this significant iron–sulphate system and may subsequently provide a new platform for related lithium battery electrode research. There is also interest in both the previously reported $Li_2Co(SO_4)_2$ phase[21] and the recently synthesized $Li_2Mn(SO_4)_2$ phase.[22]

To fully understand the factors influencing the electrochemical behaviour of the $Li_2M(SO_4)_2$ (M = Fe, Mn, Co) electrode materials, it is clear that knowledge of the fundamental solid-state properties is needed on the atomic scale. The present study uses well-established atomistic simulation and density functional theory (DFT) methods to investigate key issues related to their defect chemistry, lithium diffusion, surface structures and voltage trends. As shown in our previous studies of other lithium battery cathode materials, atomistic simulation is well suited to treating the extensive lattice relaxation around charged defects, surfaces and migrating ions in polar inorganic solids.[23–29] DFT methods[30–34] are used to provide insights into the high voltages and the local structural changes observed during electrochemical cycling of these sulphate materials.

2. Methodology

As these atomistic and DFT techniques are described in detail elsewhere,[35–37] only a general outline will be given here. For the atomistic simulations, the interatomic interactions consist of a

[a]Department of Chemistry, University of Bath, Bath, BA2 7AY, UK. E-mail: m.s.islam@bath.ac.uk
[b]Laboratoire de Réactivité et Chimie des Solides (LRCS), Université de Picardie Jules Verne, CNRS UMR 7314, 33 rue Saint Leu, 80039 Amiens Cedex, France
[c]IMPMC, CNRS UMR 7590, Université Pierre et Marie Curie UPMC Univ. Paris 06, 4 place Jussieu, 75252 Paris Cedex 05, France
[d]College de France, 11 place Marcelin Berthelot, 75231 Paris Cedex 05, France

† Electronic supplementary information (ESI) available. See DOI: 10.1039/c3ta15064j

‡ Current address: CIC Energigune, Parque Tecnológico de Álava, Albert Einstein 48, 01510 Miñano, Spain

long-range Coulombic term and a short-range component representing electron–electron repulsion and van der Waals interactions. The short-range interactions were modelled using the two-body Buckingham potential.[35] An additional three-body term was used for the SO_4^{2-} units as previously used for sulphates,[38–41] silicates[27] and phosphates.[23–25] The shell model[42] was employed to account for polarizability effects. Li–O, Fe–O and O–O interatomic potentials were taken directly from the recent study of the related *tavorite* $LiFeSO_4F$ material,[28] whilst the Mn–O and Co–O potentials were refined from those used for the study of $LiMnPO_4$ and $LiCoPO_4$.[24] For the more covalent sulphate (SO_4^{2-}) component, the interatomic potential model successfully formulated to simulate M_2SO_4 (M = Na, K, Rb and Cs) and XSO_4 (X = Sr, Ca, Ba) was used.[38–41] Table S1 (ESI†) lists the interatomic potential parameters used in this study.

As argued previously, employing these interatomic potential methods are assessed primarily by their ability to reproduce observed crystal properties. Indeed, they are found to work well, even for phosphate and silicate cathodes[23–29] where there is undoubtedly a degree of covalency. The lattice relaxation about defects (such as Li vacancies) and migrating ions was treated by the Mott–Littleton scheme incorporated in the GULP code (v4.0),[43] which partitions the crystal lattice into two regions, where ions in the inner region immediately surrounding the defect (~1000 ions) are relaxed explicitly. Hence, the polyanionic framework is not treated as a rigid lattice.

Molecular dynamics (MD) simulations were performed with DL_POLY (v2.2)[44] using the same interatomic potentials and a supercell consisting of 8 × 4 × 4 unit cells (3328 atoms) with 10% delithiation in which the lithium vacancies were initially distributed randomly. The systems were first equilibrated for at least 100 000 steps (with a time step of 0.5 fs). The main simulation runs of 2 million steps were then performed with an NPT ensemble (at $T = 473$ K) to give a long simulation time of 1 ns. NPT was used to link up with experimental conditions and slight volume changes. However, it should be noted that the large supercells and long time-scales required are currently not accessible by *ab initio* methods.

The surface structures in this study were simulated with potentials-based methods using the METADISE code.[45] Atoms near to the surface (region I) are allowed to relax while bulk atoms (region II), which represent the rest of the crystal, are kept fixed and ensure that all the ions in region I experience the forces associated with the rest of the crystal and that the energies are fully converged. The surface energy, γ, of a crystal face is defined as the excess in energy of a surface simulation over the energy of a bulk system containing the same number of atoms, per unit surface area. The equilibrium morphology of the crystal can be obtained from the surface energies using a Wulff construction in which the equilibrium form of a crystal should possess minimal total surface energy for a given volume. The surface area of a facet is not directly proportional to the surface energy. The shape would be such that the normal vector to the face from a point within the crystal would be proportional to the surface energy of that face.

DFT calculations were performed using the plane wave code VASP (v5.4).[46] Since we required optimised lattice parameters, the basis set was converged against the stress which is more sensitive to an under-converged basis set than the forces. A cutoff energy of 750 eV with a *k*-point mesh density of at least 0.04 $Å^{-1}$ was needed to adequately converge the stress (6 × 4 × 4 grid). PAW potentials[47,48] and the PBE exchange and correlation functional[49] were used. An antiferromagnetic ordering of the moments on all transition metal (Fe, Mn and Co) atoms was found to be lower in energy than a ferromagnetic ordering, in line with magnetic measurements (T_N < 8 K for $Li_2M^{II}(SO_4)_2$ with M = Co, Mn, Fe, and T_N = 35 K for $LiFe^{III}(SO_4)_2$) and with the magnetic structures deduced at 2 K from neutron powder diffraction.[22] DFT + *U* methodology was used with an effective Hubbard $U_{eff} = U - J = 4.0$, 3.9 and 5.7 eV ($J = 1.0$ eV) for Fe, Mn and Co respectively; these values are in agreement with the *U* values derived for Fe-, Mn- and Co-based cathodes.[50]

Previous DFT studies on a variety of oxide electrode materials[31,51,52] have shown that such methods are well suited to probing lithium insertion/extraction properties and to predicting precise trends in cell voltages. Using the diffraction refined structural data for the lithiated ($Li_2M(SO_4)_2$ materials) and delithiated ($LiFe(SO_4)_2$) structures we have calculated the open circuit voltages using:

$$V = \frac{\varepsilon\{Li_2M(SO_4)_2\} - \varepsilon\{Li_xM(SO_4)_2\} - \{2-x\}\mu\{Li\}}{2-x} \quad (1)$$

where $\varepsilon\{Y\}$ is the total energy of *Y* and *x* is the number of lithium atoms per formula unit removed. In practice we have removed one lithium atom per formula unit to produce the end member $LiM(SO_4)_2$ (M = Fe, Mn, Co). Bulk lithium was used to calculate the chemical potential of a single lithium atom $\mu\{Li\}$, which is standard practice for cell voltage calculations.

3. Results and discussion

3.1 Structures and intrinsic defects

The structures of the monoclinic $Li_2M(SO_4)_2$ (M = Co, Mn, Fe) compounds have previously been reported,[21,22] and the atomic positions and unit cell parameters are collected in Table S2.† This structure comprises isolated MO_6 octahedra linked through shared oxygen vertices with the surrounding SO_4 tetrahedra. Each octahedron is linked to six SO_4 tetrahedra which are orientated in a star or pinwheel pattern when viewed along the *b*-axis. Conversely, each SO_4 is only bound to three MO_6 octahedra and the fourth unshared corner of the SO_4 tetrahedron points into an open channel where the lithium resides, as shown in Fig. 1.

Despite the isostructural nature of the three $Li_2M(SO_4)_2$ phases, only the Fe analogue is observed to be electrochemically active.[21,22] Upon cycling, the $Li_2Fe(SO_4)_2$ material transforms to the delithiated phase $LiFe(SO_4)_2$ through a biphasic mechanism, as suggested by the plateau observed at 3.83 V *vs.* Li/Li^+ on the electrochemical curve and further confirmed by *in situ* XRD measurements.[21] The delithiated phase $LiFe(SO_4)_2$ can also be obtained through chemical oxidation of $Li_2Fe(SO_4)_2$. It was found that the delithiated phase maintains the general 3D framework of $Li_2Fe(SO_4)_2$,[22] but the FeO_6 octahedra and SO_4 tetrahedra undergo slight rotations upon lithium removal. As a

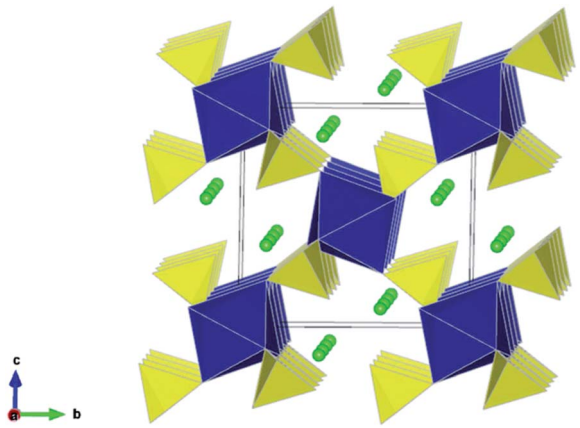

Fig. 1 $Li_2M(SO_4)_2$ (M = Fe, Mn, Co) crystal structure showing MO_6 octahedra (blue), SO_4 tetrahedra (yellow) and chains of Li ions (green) running parallel to the *a*-axis. [Experimental refinement data in Table S2.†]

result, each octahedron is still linked to six SO_4 tetrahedra with the fourth unshared corner of the SO_4 tetrahedra pointing at the open channels where the lithium resides. However, in contrast to the lithiated phase, the lithium ions of the oxidized $LiFe(SO_4)_2$ were localized at the centre of the channels, in a half-occupied general position in the vicinity of the (1/2 0 1/2) site.[22] The lower panel of Table S2† presents the precise atomic positions obtained from a joint refinement of the synchrotron XRD and NPD data,[22] and Fig. 2 shows the resulting crystal structure.

The starting point of the simulation study was to reproduce the experimentally observed crystal structures exhibited by the $Li_2M(SO_4)_2$ (M = Fe, Mn, Co) electrode materials. A direct comparison of their calculated and experimental structures is given in Table 1, which shows that the unit cell parameters calculated by interatomic potentials deviate from the experiment by at most 0.1 Å, and in most cases by much less; the same is found for the individual bond lengths with mean deviations less than 0.03 Å. The successful reproduction of these complex

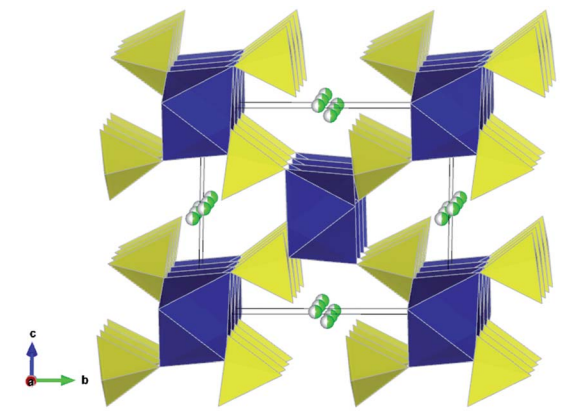

Fig. 2 Crystal structure of the delithiated phase $LiFe(SO_4)_2$ showing FeO_6 octahedra (blue), SO_4 tetrahedra (yellow) and half occupied Li sites (green/white) running parallel to the *a*-axis. [Experimental refinement data in Table S2.†]

Table 1 Comparison of the calculated (potentials-based) and experimental structural parameters of $Li_2M(SO_4)_2$ (M = Fe, Mn, Co)

Parameter	*a* (Å)	*b* (Å)	*c* (Å)	*β* (°)
$Li_2Fe(SO_4)_2$				
Calc.	4.9518	8.2212	8.9293	121.86
Expt.[21]	4.9886	8.2062	8.8293	121.75
Δ	−0.0368	0.0150	0.1000	0.11
$Li_2Mn(SO_4)_2$				
Calc.	4.9478	8.2930	8.9456	121.58
Expt.[22]	4.9920	8.3396	8.8614	121.23
Δ	−0.0442	−0.0466	0.0842	0.35
$Li_2Co(SO_4)_2$				
Calc.	4.9596	8.0875	8.8142	121.37
Expt.[21]	4.9787	8.1113	8.7831	121.81
Δ	0.0191	0.0238	0.0311	−0.44

sulphate structures gives us confidence that the potential models can be used reliably for subsequent defect, diffusion and surface calculations.

As noted, insight into the defect properties of cathode materials is crucial to the full understanding of their electrochemical behaviour. Isolated point defect (vacancy and interstitial) energies were calculated for these sulphate systems, which were combined to determine the formation energies for Frenkel- and Schottky-type intrinsic defects. The following equations represent the reactions involving these defects (using Kröger–Vink notation and where M = Fe, Mn or Co):

$$\text{Li Frenkel}: \ \mathrm{Li}_{\mathrm{Li}}^{\times} \rightarrow \mathrm{V}'_{\mathrm{Li}} + \mathrm{Li}_{\mathrm{i}}^{\cdot} \quad (2)$$

$$\text{M Frenkel}: \ \mathrm{M}_{\mathrm{M}}^{\times} \rightarrow \mathrm{V}''_{\mathrm{M}} + \mathrm{M}_{\mathrm{i}}^{\cdot\cdot} \quad (3)$$

$$\text{Schottky}: \ 2\mathrm{Li}_{\mathrm{Li}}^{\times} + \mathrm{M}_{\mathrm{M}}^{\times} + 2\mathrm{S}_{\mathrm{S}}^{\times} + 8\mathrm{O}_{\mathrm{O}}^{\times} \rightarrow 2\mathrm{V}'_{\mathrm{Li}} + \mathrm{V}''_{\mathrm{M}} + 2\mathrm{V}_{\mathrm{S}}^{''''''} + 8\mathrm{V}_{\mathrm{O}}^{\cdot\cdot} + \mathrm{Li}_2\mathrm{M}(\mathrm{SO}_4)_2 \quad (4)$$

We also examined the Li/M "anti-site" pair defect, which involves the exchange of an Li^+ ion (radius 0.76 Å) with an M^{2+} ion (Fe^{2+} radius 0.78 Å, Mn^{2+} radius 0.83 Å, and Co^{2+} radius 0.75 Å), according to:

$$\text{Li/M antisite}: \ \mathrm{Li}_{\mathrm{Li}}^{\times} + \mathrm{M}_{\mathrm{M}}^{\times} \rightarrow \mathrm{Li}'_{\mathrm{M}} + \mathrm{M}_{\mathrm{Li}}^{\cdot} \quad (5)$$

This type of defect is worth investigating since Li/M anti-site or cation exchange effects have been found in other polyanionic systems including $LiMPO_4$ (M = Mn, Fe, Co, Ni)[23,24] and $Li_2FeP_2O_7$.[29]

Examination of the resulting defect energies listed in Table 2 reveals two main predictions. First, the formation of all Frenkel and Schottky defects is unfavourable in all $Li_2M(SO_4)_2$ structures. This suggests that the creation of vacancies (especially oxygen vacancies) and interstitial defects are unfavourable on energetic grounds. Second, the antisite energies are also relatively high, which suggests that there would be no significant concentration of M on Li sites at typical operating temperatures in these fluorine-free sulphate materials, and is consistent with

Table 2 Energies of intrinsic atomic defect processes in $Li_2M(SO_4)_2$ (M = Fe, Mn, Co)

		Energy (eV)		
Disorder type	Eqn	$Li_2Fe(SO_4)_2$	$Li_2Mn(SO_4)_2$	$Li_2Co(SO_4)_2$
Li Frenkel	(2)	3.77	3.54	3.51
M Frenkel	(3)	9.88	10.14	9.26
Schottky	(4)	20.96	19.92	19.51
Li/M antisite	(5)	3.92	3.65	3.50

Table 3 Activation energies for Li migration paths (illustrated in Fig. 3) for $Li_2M(SO_4)_2$ (M = Fe, Mn, Co)

	Activation energy (eV)		
Path	$Li_2Fe(SO_4)_2$	$Li_2Mn(SO_4)_2$	$Li_2Co(SO_4)_2$
L1	0.33	0.39	0.32
L2	1.61	1.58	1.20
L3	1.72	1.93	1.77
L4	0.47	0.54	0.42
L5	1.79	1.74	1.98

the experimental data. This result contrasts with the $LiMPO_4$ (M = Mn, Fe, Co and Ni) materials,[23,53,54] which exhibit cation exchange behaviour between M and Li sites. The contrast may be related to differences in structure and in the bonding of the polyanion groups. Therefore these results suggest that conduction "blocking" effects involving Fe, Mn or Co on Li sites are much less likely in the $Li_2M(SO_4)_2$ cathode materials.

3.2 Lithium diffusion paths

To fully understand charge/discharge rates of potential cathodes, it is important to examine the energy barriers and dimensionality of lithium diffusion. Using atomistic simulation techniques, it is possible to examine various possible Li^+ transport paths, which are often difficult to probe on the atomic scale by experiment alone.

Five possible migration paths in the sulphate structures were examined, including all possible jumps between adjacent lithium sites, which are symmetry equivalent; these paths are labelled L1–L5 in Fig. 3. Activation energies for these migration paths can be derived by calculating the energy of the migrating ion along the diffusion path, and are listed in Table 3.

The calculated activation energies reveal two main points. First, for all sulphates, the paths with lowest migration energies are found to be the L1 and L4 jumps. The results indicate that combinations of the L1 and L4 pathways consists of continuous diagonal or zigzag jumps enabling long-range diffusion along the [100] direction, *i.e.* along the *a*-axis channels (Fig. 4a and b). The net diffusion barriers are 0.47 eV, 0.54 eV and 0.42 eV for $Li_2Fe(SO_4)_2$, $Li_2Mn(SO_4)_2$, and $Li_2Co(SO_4)_2$ respectively. We note that as with other battery cathode materials, there is no clear correlation between the Li–Li jump distances (Table S3†) and the migration barriers are largely due to the different local structural and steric factors at the saddle-point configuration.

Secondly, we note that the remaining Li migration paths considered (L2, L3 and L5) were found to have high and unfavourable activation energies (≥1.2 eV); this is probably due to the migrating Li ion coming into close proximity of the MO_6 octahedra. Hence it would appear that the $Li_2M(SO_4)_2$ materials exhibit effective 1D transport of Li ions. We have determined experimentally the conduction activation energy in $Li_2Fe(SO_4)_2$ by AC-conductivity performed on a sintered pellet using blocking electrodes within the 200–350 °C temperature range and found from linear extrapolation a value of ~1.1 eV. This

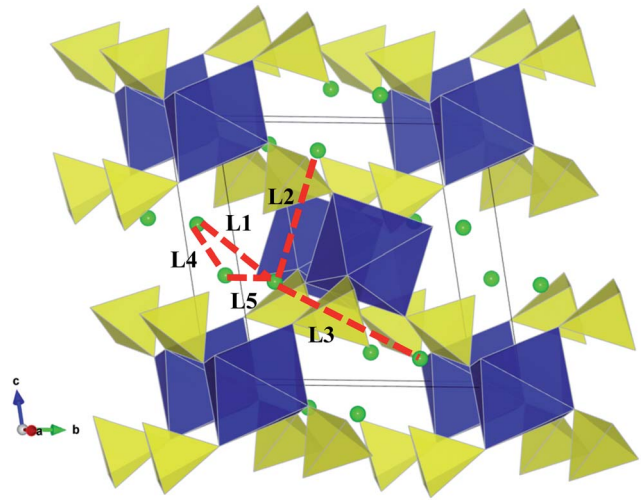

Fig. 3 Lithium ion migration paths in $Li_2M(SO_4)_2$ (M = Fe, Mn, Co) between adjacent Li sites (with initial Li positions found in Table S2†). Li–Li jumps considered are labelled L1–L5 (with Li–Li separations found in Table S3†).

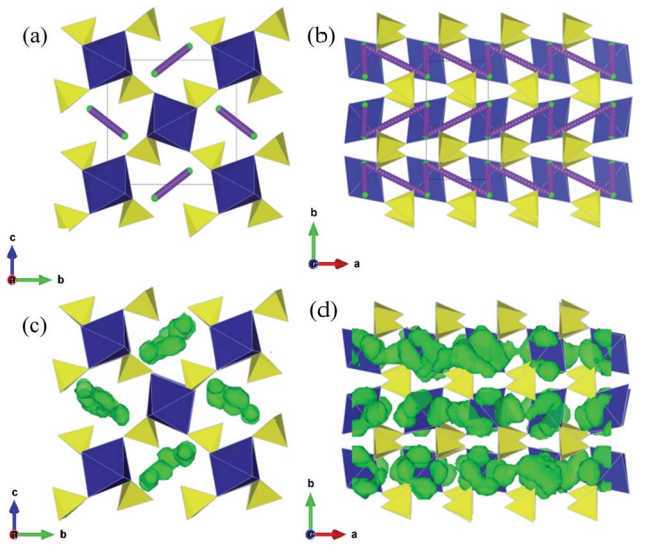

Fig. 4 Low energy Li diffusion paths within [100] channels of $Li_2M(SO_4)_2$ (M = Fe, Mn, Co). (a) and (b) Static lattice calculations of low energy Li migration path combining L1 and L4 jumps. (c) and (d) Li density plots as calculated using MD at 473 K. (a), (c) and (b), (d) are equivalent views along the *a*-axis and *c*-axis respectively.

corresponds to the total conductivity of pristine stoichiometric $Li_2Fe(SO_4)_2$ and will comprise both ionic and electronic conductivity terms. Hence direct comparison between this measured conductivity value and the calculated migration energies for Li ion conduction (using Li vacancy sites) is not straightforward. Despite the difference, our simulations have elucidated the pathways and dimensionality of Li ion diffusion, which are the main aims of this study.

To complement the energy minimisation calculations, molecular dynamics (MD) simulations were performed to examine the Li ion diffusion pathways and dimensionality within the sulphate structures. Scatter or density plots of Li ion coordinates over the simulation timescale enable the migration paths and the regions of the structure most frequently traversed to be visualized.

Fig. 4c and d show the location of the Li density found from the simulation runs; this confirms the prediction of our static lattice calculations that Li diffusion will occur *via* a combination of the L1 and L4 jumps and thus allow long-range 1D diffusion along the [100] direction. As noted, Li/M antisite disorder is energetically unfavourable in these sulphates, and hence the 1D Li^+ diffusion is much less likely to be hindered by such defects. The MD simulations also confirm that Li diffusion involves conventional hopping between Li sites with no evidence of cooperative 'knock-on' mechanisms.

3.3 Surfaces and particle morphology

The particle morphology is important because for facile lithium insertion/extraction the predicted 1D conduction channels must terminate at a low energy surface facet. However, direct experimental measurements on surface structures of the sulphates have not been carried out.

We initially focus on the Fe-based material as a model system and due to its superior electrochemical activity. Thirteen low index crystal facets and their symmetry related equivalent surfaces of $Li_2Fe(SO_4)_2$ have been modelled for the first time and the resulting surface energies are listed in Table 4. Due to the highly interconnected nature of the FeO_6 and SO_4 polyhedra, there are no simple planar cuts that are non-polar. In all cases the layers must be reconstructed in order to remove the dipole.

Table 4 Calculated surface properties of $Li_2Fe(SO_4)_2$

Surface	Surface energy (J m^{-2})	Surface area in morphology (%)
{011}	0.68	65.5
{102}	0.86	2.2
{112}	0.87	0.4
{111}	0.88	1.5
{001}	0.90	1.0
{210}	0.90	27.1
{121}	0.92	2.3
{122}	0.93	0.0
{211}	0.93	0.0
{101}	0.95	0.0
{100}	0.95	0.0
{010}	1.01	0.0
{221}	1.03	0.0

Using these calculated surface energies a Wulff construction of the equilibrium morphology has been made which reveals a rhombohedral-like shape (Fig. 5). For small crystals where rearrangement of the crystal at each stage of the growth process is possible, a morphology close to the equilibrium form would be expected. However, there are no published indexed TEM images of $Li_2Fe(SO_4)_2$ for direct comparison; indeed, such comparison is not trivial due to different experimental synthesis methods and possible non-equilibrium conditions. Nevertheless, our focus here is to reveal new information on the surface facets that are exposed, which are significant for lithium extraction/insertion processes.

The {011} facet has the lowest surface energy at 0.68 J m^{-2} and makes up two thirds (65.5%) of the overall surface area of the particle (shown in blue in Fig. 5a). The {210} surface is the next most dominant surface comprising 27% of the surface area (shown in red in Fig. 5b). Earlier in this study we showed that the facile direction for lithium migration is along the channels in the [100] direction. Both the {210} and {102} facets expose these channels (Fig. 5c). It is well known that the growth environment can have a significant effect upon the morphology of a particle and it may be possible to increase the surface area that allows facile Li access by alteration of the synthesis conditions.

Having predicted the dominance of the {011} and {210} surfaces in the morphology, we present details of both relaxed surface structures in Fig. 6. A useful quantity here is the relaxation energy, which is the difference between the unrelaxed surface energy of the crystal cleaved from the bulk and the final relaxed surface energy. This quantity gives a measure of the degree of structural change in the surface region as the surface is formed. Structural relaxations in the {011} surface are small which is reflected in the relaxation energy of 0.16 J m^{-2}. The largest relaxations occur in the topmost layer and these are associated with a small rotation of the terminal SO_4 units, which causes an inward displacement of 0.43 Å of the oxygen

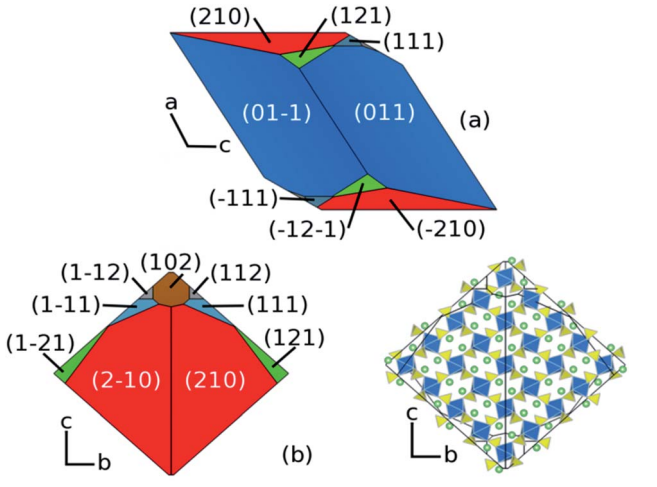

Fig. 5 Calculated particle morphology of $Li_2Fe(SO_4)_2$; as viewed along (a) the *b*-axis, (b) the *a*-axis. In (c) the atomic structure is overlaid upon the *a*-axis view showing the availability of access to the 1D migration channels.

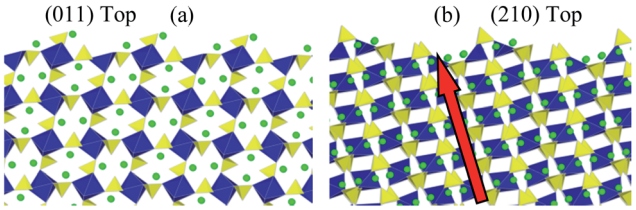

Fig. 6 Side view of relaxed (a) {011} and (b) {210} surfaces of $Li_2Fe(SO_4)_2$. The red arrow indicates the Li migration direction for {210} towards the outermost surface. For the {011} surface Li migration is into the page.

ion at the outer vertex and an inward displacement of 0.13 Å of the Li atom that is adjacent to this. There are 50% lithium vacancies in the topmost layer and half of the SO_4 tetrahedra are absent which gives rise to a degree of rumpling.

By contrast there is significant relaxation at the {210} surface with a large relaxation energy of 1.79 J m^{-2}. Some loss of coordination is present in all of the terminal FeO_6 octahedra and the terminal SO_4 units undergo significant tilting. The near surface Li move outwards by up to 1 Å to form part of the terminal layer. As indicated in Fig. 6b, the prominence of the {210} surface is significant since it exposes the facile pathway for lithium ion conduction (along the [100] channel), and hence is important for the reversible insertion/de-insertion of lithium ions.

3.4 Cell voltage trends

As with the potentials-based calculations, the DFT simulations have reproduced the $Li_2M(SO_4)_2$ (M = Fe, Mn, Co) experimental structures and also the delithiated $LiFe(SO_4)_2$ observed structure with a high level of accuracy (Tables S4 and S5†). The computed cell voltage relies on a knowledge of the structure of the delithiated end member $LiFe(SO_4)_2$. Typically for cell voltage calculations the relevant lithium atoms are removed directly from the lithiated structure, which is then energy minimised to form the delithiated structure. Numerous configurations of differing lithium ordering schemes were considered, and in our calculations we used the lowest energy structure. However, this energy minimisation may only find the local energy minimum and it is entirely possible that a phase change can occur on lithium extraction.

The cell voltage computed directly in this way for $Li_2Fe(SO_4)_2$ is 3.99 V which is in reasonable agreement with the measured voltage of 3.83 V.[21] However, using the joint Synchrotron XRD/neutron refined $LiFe(SO_4)_2$ structure (Table S2†), it is clear that the main difference between the lithiated and delithiated materials is that in the $Li_2Fe(SO_4)_2$ structure there are two rows of lithium in a zig-zag arrangement whereas in the $LiFe(SO_4)_2$ structure (Fig. 2) there are half-occupied Li sites in the channel. This subtle change in the structure results in a computed cell voltage of 3.91 V, which is in better agreement with that measured experimentally (Table 5). This result highlights the effect of structural changes on lithium removal and their importance in cell voltage computations.

Table 5 Calculated cell voltages (*vs.* Li/Li^+) in $Li_2M(SO_4)_2$ (M = Fe, Mn, Co)

Process	Expt.[21] (V)	Calc. (V)
$Li_2Fe(SO_4)_2 \leftrightarrow LiFe(SO_4)_2$	3.83	3.91
$Li_2Mn(SO_4)_2 \leftrightarrow LiMn(SO_4)_2$	—	4.54
$Li_2Co(SO_4)_2 \leftrightarrow LiCo(SO_4)_2$	—	5.20

Having isolated the delithiated ($LiFe(SO_4)_2$) structure we have subsequently calculated voltages for the Mn- and Co-based sulphates by setting both $LiMn(SO_4)_2$ and $LiCo(SO_4)_2$ initial structures equivalent to $LiFe(SO_4)_2$ prior to structural relaxation. The voltages calculated for $Li_2M(SO_4)_2$ (M = Fe, Mn, Co) are presented in Table 5.

Our calculations suggest that both $Li_2Mn(SO_4)_2$ and $Li_2Co(SO_4)_2$ have higher cell voltages than that of $Li_2Fe(SO_4)_2$ as typically observed for polyanion cathodes. The value for the Co-based sulphate is above the electrolyte stability window. Such a significant shift upwards in voltage is found for other Co-polyanion compounds, such as $LiCoPO_4$ for which a voltage of 4.8 V *vs.* Li/Li^+ has been observed[3,55] in comparison to 3.4 V for $LiFePO_4$.

The Mn-based sulphate is known to be electrochemically inactive. As the system is delithiated, Mn^{3+} (d^4) forms which is a Jahn–Teller active valence state. It has been debated whether Jahn–Teller distortion of the MnO_6 octahedra could lead to non-uniform structural distortions which will render the delithiated phase unstable and thus unable to form. Such effects are well known in other Mn-based battery materials.[56,57] GGA + *U* calculations provide a useful probe of local structural distortions that are not affected by thermal motion and statistical averaging over many unit cells. To check for Jahn–Teller effects we have examined the MO_6 distortion in the Fe, Co and Mn based sulphates, which is presented in Table 6. For this we have used the Baur[58] distortion coefficient, *D*, which is defined as:

$$D = \frac{1}{n}\sum_{i=1}^{n}\frac{|l_i - l_{av}|}{l_{av}} \quad (6)$$

where l_i is the distance from the central atom to the i^{th} coordinating atom, and l_{av} is the average bond length to *n* coordinating atoms.

The data in Table 6 indicate that all the lithiated structures $Li_2Fe(SO_4)_2$, $Li_2Mn(SO_4)_2$ and $Li_2Co(SO_4)_2$ possess a similar low

Table 6 Calculated M–O bond lengths and MO_6 octahedral distortion in $Li_2M(SO_4)_2$ and delithiated $LiM(SO_4)_2$ (where M = Fe, Mn, Co)

Material	Mean M–O bond length (Å)	MO_6 distortion coefficient ($\times 10^{-2}$)
$Li_2Fe(SO_4)_2$	2.15	1.8
$LiFe(SO_4)_2$	2.01	1.4
$Li_2Mn(SO_4)_2$	2.21	2.0
$LiMn(SO_4)_2$	2.08	7.2
$Li_2Co(SO_4)_2$	2.12	1.6
$LiCo(SO_4)_2$	2.01	2.0

degree of distortion. Upon delithiation there is a large increase in the MnO_6 distortion with a coefficient of 7.2×10^{-2} (compared to 1.4×10^{-2} and 2.0×10^{-2} for FeO_6 and CoO_6 respectively). Since the Mn-based sulphate is electrochemically inactive, the calculated voltage presented in Table 5 assumes the same delithiated starting structure as the Co and Fe based sulphates, but contains cooperative Jahn–Teller distortion after structure relaxation. Further work to determine if such structural distortion in this phase leads to mechanical instability is on-going including phonon spectrum simulations.

A possible source of the different cell voltages for $Li_2M(SO_4)_2$ (M = Fe, Mn, Co) is in the relative strength of the corresponding Fe^{2+}/Fe^{3+}, Mn^{2+}/Mn^{3+} and Co^{2+}/Co^{3+} redox couples. As with other systems involving M^{2+}/M^{3+} redox couples we would expect the respective M–O bond lengths to shorten upon Li removal (oxidation) within these sulphate systems. This is indeed found with the Fe–O bond lengths contracting by ~6.5% (from 2.15 Å to 2.01 Å), the Mn–O bond lengths contracting by ~6% (from 2.21 Å to 2.08 Å) and the Co–O bond lengths contracting by ~5% (from 2.12 Å to 2.01 Å).

However, distinguishing among the most reliable parameters to account for voltage variation is not an easy task. The voltage also depends upon other factors such as: inductive effects of SO_4, PO_4 and SiO_4; the degree of ionic or covalent character of the cation–anion bonds; and the Madelung energy of the ionic component of the bonding. As discussed previously,[2,59] another possibility relates to the inductive effect played by lithium. There are obviously hidden issues which remain to be unravelled, and are part of on-going studies.

4. Conclusions

This systematic survey of the $Li_2M(SO_4)_2$ (M = Fe, Mn, Co) cathode materials has used a combination of atomistic simulation and DFT techniques to provide insights into the defect chemistry, Li diffusion paths, crystal morphologies and voltage trends. The key results can be summarized as follows:

(1) The atomistic simulations of $Li_2M(SO_4)_2$ (M = Fe, Mn, Co) show good reproduction of their observed structures. The defect calculations indicate that the formation of all Frenkel, Schottky and Li/M anti-site intrinsic defects is unfavourable for all phases. In particular, the results suggest there would be no significant intrinsic anti-site defect concentration of Fe, Mn or Co on Li sites at typical operating temperatures within these sulphates. This is in contrast to the $LiFePO_4$ material, which has a small amount of Fe on Li sites.

(2) Lithium diffusion simulations reveal low migration energies (~0.4–0.5 eV) along the *a*-axis channels of $Li_2Fe(SO_4)_2$, $Li_2Mn(SO_4)_2$ and $Li_2Co(SO_4)_2$ suggesting 1D diffusion and good Li mobility which is important for favourable rate capability. MD calculations verify the 1D migration pathways along the *a*-axis channels, with no evidence of cooperative mechanisms.

(3) The calculated equilibrium morphology of $Li_2Fe(SO_4)_2$ adopts a rhombohedral-like shape with {011} and {210} surfaces dominating. The prominence of the {210} surface is significant since it allows access to the facile pathway for lithium ion conduction (along the [100] channel), and hence is important for the reversible insertion/de-insertion of lithium ions.

(4) The calculated cell voltage (3.91 V) for $Li_2Fe(SO_4)_2$ is in excellent agreement with that determined experimentally (3.83 V). Characterisation of the experimental structure of the delithiated $LiFe(SO_4)_2$ phase was found to be important in this agreement. $Li_2Mn(SO_4)_2$ is known to be electrochemically inactive and the predicted voltage for $Li_2Co(SO_4)_2$ was found to be 5.20 V, which may be beyond the stability range of the current electrolyte.

Acknowledgements

This work was funded by the EPSRC Supergen programme and made use of the high-performance computing service HECToR, *via* the HPC Materials Chemistry Consortium. M.R. acknowledges the French "Ministère de l'Enseignement Supérieur et de la Recherche" for her Ph.D. Grant, and thanks Loïc Dupont and Charles Delacourt for fruitful discussions.

Notes and references

1 M. Armand and J. M. Tarascon, *Nature*, 2008, **451**, 652.
2 J. B. Goodenough and Y. Kim, *Chem. Mater.*, 2010, **22**, 587.
3 B. L. Ellis, K. T. Lee and L. F. Nazar, *Chem. Mater.*, 2010, **22**, 691.
4 M. R. Palacin, *Chem. Soc. Rev.*, 2009, **38**, 2565.
5 C. Masquelier and L. Croguennec, *Chem. Rev.*, 2013, **113**, 6552.
6 V. Etacheri, R. Marom, R. Elazari, G. Salitra and D. Aurbach, *Energy Environ. Sci.*, 2011, **4**, 3243.
7 Z. L. Gong and Y. Yang, *Energy Environ. Sci.*, 2011, **4**, 3223.
8 A. K. Padhi, K. S. Nanjundaswamy and J. B. Goodenough, *J. Electrochem. Soc.*, 1997, **144**, 1188.
9 A. Nyten, A. Abouimrane, M. Armand, T. Gustafsson and J. O. Thomas, *Electrochem. Commun.*, 2005, **7**, 156.
10 M. S. Islam, R. Dominko, C. Masquelier, C. Sirisopanaporn, A. R. Armstrong and P. G. Bruce, *J. Mater. Chem.*, 2011, **21**, 9811.
11 A. Yamada, N. Iwane, Y. Harada, S. Nishimura, Y. Koyama and I. Tanaka, *Adv. Mater.*, 2010, **22**, 3583.
12 N. Recham, J. N. Chotard, L. Dupont, C. Delacourt, W. Walker, M. Armand and J. M. Tarascon, *Nat. Mater.*, 2010, **9**, 68.
13 P. Barpanda, M. Ati, B. C. Melot, G. Rousse, J. N. Chotard, M. L. Doublet, M. T. Sougrati, S. A. Corr, J. C. Jumas and J. M. Tarascon, *Nat. Mater.*, 2011, **10**, 772; R. Tripathi, T. N. Ramesh, B. L. Ellis and L. F. Nazar, *Angew. Chem. Int. Ed.*, 2010, **49**, 8738.
14 M. Ati, B. C. Melot, J. N. Chotard, G. Rousse, M. Reynaud and J. M. Tarascon, *Electrochem. Commun.*, 2011, **13**, 1280.
15 G. Rousse and J. M. Tarascon, *Chem. Mater.*, 2014, **26**, 394.
16 B. L. Ellis, W. R. M. Makahnouk, Y. Makimura, K. Toghill and L. F. Nazar, *Nat. Mater.*, 2007, **6**, 749.
17 S. Nishimura, M. Nakamura, R. Natsui and A. Yamada, *J. Am. Chem. Soc.*, 2010, **132**, 13596.

18 C. V. Subban, M. Ati, G. Rousse, A. M. Abakumov, G. Van Tendeloo, R. Janot and J. M. Tarascon, *J. Am. Chem. Soc.*, 2013, **135**, 3653.
19 M. A. Reddy, V. Pralong, V. Caignaert, U. V. Varadaraju and B. Raveau, *Electrochem. Commun.*, 2009, **11**, 1807.
20 M. A. Gomez, G. Ventruti, M. Celikin, H. Assaaoudi, H. Putz, L. Becze, K. E. Lee and G. P. Demopoulos, *RSC Adv.*, 2013, **3**, 16840.
21 M. Reynaud, M. Ati, B. C. Melot, M. T. Sougrati, G. Rousse, J. N. Chotard and J. M. Tarascon, *Electrochem. Commun.*, 2012, **21**, 77.
22 M. Reynaud, G. Rousse, J. N. Chotard, J. Rodriguez-Carvajal and J. M. Tarascon, *Inorg. Chem.*, 2013, **52**, 10456.
23 M. S. Islam, D. J. Driscoll, C. A. J. Fisher and P. R. Slater, *Chem. Mater.*, 2005, **17**, 5085.
24 C. A. J. Fisher, V. M. H. Prieto and M. S. Islam, *Chem. Mater.*, 2008, **20**, 5907.
25 G. R. Gardiner and M. S. Islam, *Chem. Mater.*, 2010, **22**, 1242.
26 C. A. J. Fisher and M. S. Islam, *J. Mater. Chem.*, 2008, **18**, 1209.
27 A. R. Armstrong, N. Kuganathan, M. S. Islam and P. G. Bruce, *J. Am. Chem. Soc.*, 2011, **133**, 13031.
28 R. Tripathi, G. R. Gardiner, M. S. Islam and L. F. Nazar, *Chem. Mater.*, 2011, **23**, 2278.
29 J. M. Clark, S. Nishimura, A. Yamada and M. S. Islam, *Angew. Chem., Int. Ed.*, 2012, **51**, 13149.
30 C. Eames, A. R. Armstrong, P. G. Bruce and M. S. Islam, *Chem. Mater.*, 2012, **24**, 2155.
31 F. Zhou, M. Cococcioni, C. A. Marianetti, D. Morgan and G. Ceder, *Phys. Rev. B: Condens. Matter Mater. Phys.*, 2004, **70**, 23.
32 H. Zhou, S. Upreti, N. A. Chernova, G. Hautier, G. Ceder and M. S. Whittingham, *Chem. Mater.*, 2011, **23**, 293.
33 A. R. Armstrong, C. Lyness, P. M. Panchmatia, M. S. Islam and P. G. Bruce, *Nat. Mater.*, 2011, **10**, 223.
34 D. A. Tompsett and M. S. Islam, *Chem. Mater.*, 2013, **25**, 2515.
35 A. Walsh, A. A. Sokol and C. R. A. Catlow, in *Computational Approaches to Energy Materials*, Wiley-Blackwell, 2013.
36 M. S. Islam and C. A. J. Fisher, *Chem. Soc. Rev.*, 2014, **43**, 185.
37 W. Koch and M. C. Holthausen, in *A Chemist's Guide to Density Functional Theory*, Wiley-VCH Verlag GmbH, Weinheim, 2001.
38 N. L. Allan, A. L. Rohl, D. H. Gay, C. R. A. Catlow, R. J. Davey and W. C. Mackrodt, *Faraday Discuss.*, 1993, **95**, 273.
39 S. E. Redfern and S. C. Parker, *J. Chem. Soc., Faraday Trans.*, 1998, **94**, 1947.
40 G. Sastre and J. D. Gale, *Chem. Mater.*, 2005, **17**, 730.
41 L. Gomez-Hortiguela, F. Cora, C. R. A. Catlow and J. Perez-Pariente, *J. Am. Chem. Soc.*, 2004, **126**, 12097.
42 B. G. Dick and A. W. Overhauser, *Phys. Rev.*, 1958, **112**, 90.
43 J. D. Gale and A. L. Rohl, *Mol. Simul.*, 2003, **29**, 291.
44 W. Smith and T. R. Forester, *J. Mol. Graphics*, 1996, **14**, 136.
45 G. W. Watson, E. T. Kelsey, N. H. deLeeuw, D. J. Harris and S. C. Parker, *J. Chem. Soc., Faraday Trans.*, 1996, **92**, 433.
46 G. Kresse and J. Furthmuller, *Phys. Rev. B: Condens. Matter Mater. Phys.*, 1996, **54**, 11169.
47 P. E. Blochl, *Phys. Rev. B: Condens. Matter Mater. Phys.*, 1994, **50**, 17953.
48 G. Kresse and D. Joubert, *Phys. Rev. B: Condens. Matter Mater. Phys.*, 1999, **59**, 1758.
49 J. P. Perdew, K. Burke and M. Ernzerhof, *Phys. Rev. Lett.*, 1996, **77**, 3865.
50 T. Mueller, G. Hautier, A. Jain and G. Ceder, *Chem. Mater.*, 2011, **23**, 3854.
51 G. Ceder, M. K. Aydinol and A. F. Kohan, *Comput. Mater. Sci.*, 1997, **8**, 161.
52 C. Arrouvel, S. C. Parker and M. S. Islam, *Chem. Mater.*, 2009, **21**, 4778.
53 J. Maier and R. Amin, *J. Electrochem. Soc.*, 2008, **155**, A339.
54 J. J. Chen, M. J. Vacchio, S. J. Wang, N. Chernova, P. Y. Zavalij and M. S. Whittingham, *Solid State Ionics*, 2008, **178**, 1676.
55 K. Amine, H. Yasuda and M. Yamachi, *Electrochem. Solid State Lett.*, 2000, **3**, 178.
56 A. Van der Ven, C. Marianetti, D. Morgan and G. Ceder, *Solid State Ionics*, 2000, **135**, 21.
57 M. M. Thackeray, W. I. F. David, P. G. Bruce and J. B. Goodenough, *Mat. Res. Bull.*, 1983, **18**, 461.
58 W. H. Baur, *Acta Crystallogr., Sect. B: Struct. Sci.*, 1974, **30**, 1195.
59 B. C. Melot, D. Scanlon, M. Reynaud, M. Ati, G. Rousse, J. N. Chotard, M. Henry and J. M. Tarascon, *ACS Appl. Mater. Interfaces*, 2014, DOI: 10.1021/am405579h.